Experimental Research

INTERNATIONAL JOURNAL OF SURGERY

OPEN

An anti-infection and biodegradable TFRD-loaded porous scaffold promotes bone regeneration in segmental bone defects: experimental studies

Haixiong Lin, PhD, MD[a,b,c], Zige Li, MMed[h], Zhenze Xie, PhD[d], Shengyao Tang, MMed[e], Minling Huang, MMed[n], Junjie Feng, MMed[m], Yuhan Wei, MBBS[i], Zhen Shen, PhD, MD[j], Ruoyu Zhou, MMed[k], Yuanlan Feng, MMed[l], Huamei Chen, MMed[f], Yueyi Ren, PhD, MD[c], Feng Huang, MMed[g], Xiaotong Wang, PhD, MD[i,*], Ziwei Jiang, PhD, MD[g,*]

Background: Addressing segmental bone defects remains a complex task in orthopedics, and recent advancements have led to the development of novel drugs to enhance the bone regeneration. However, long-term oral administration can lead to malnutrition and poor patient compliance. Scaffolds loaded with medication are extensively employed to facilitate the restoration of bone defects.
Methods: Inspired by the local application of total flavonoids of *Rhizoma Drynariae* (TFRD) in the treatment of fracture, a novel 3D-printed HA/CMCS/PDA/TFRD scaffold with anti-infection, biodegradable and induced angiogenesis was designed, and to explore its preclinical value in segmental bone defect of tibia.
Results: The scaffold exhibited good degradation and drug release performance. In vitro, the scaffold extract promoted osteogenesis by enhancing bone-related gene/protein expression and mineral deposition in BMSCs. It also stimulated endothelial cell migration and promoted angiogenesis through the upregulation of specific genes and proteins associated with cell migration and tube formation. This may be attributed to the activation of the PI3k/AKT/HIF-1α pathway, facilitating the processes of osteogenesis and angiogenesis. Furthermore, the HA/CMCS/PDA/TFRD scaffold was demonstrated to alleviate infection, enhance angiogenesis, promote bone regeneration, and increase the maximum failure force of new formed bone in a rat model of segmental bone defects.
Conclusion: Porous scaffolds loaded with TFRD can reduce infection, be biodegradable, and induce angiogenesis, presenting a novel approach for addressing tibial segmental bone defects.

Keywords: angiogenesis, bone defect, bone microenvironment, drug delivery scaffold

[a]Center for Neuromusculoskeletal Restorative Medicine, Institute for Tissue Engineering and Regenerative Medicine, The Chinese University of Hong Kong, Hong Kong SAR, [b]Department of Orthopaedics, Ningxia Hui Autonomous Region Hospital and Research Institute of Traditional Chinese Medicine, Yinchuan, [c]The First School of Clinical Medicine, Guangzhou University of Chinese Medicine, [d]Department of Biomedical Engineering, School of Materials Science and Engineering, South China University of Technology, [e]Department of Orthopaedics, Guangdong Provincial Second Hospital of Traditional Chinese Medicine, Guangdong Provincial Key Laboratory of Research and Development in Traditional Chinese Medicine, Guangdong Provincial Engineering Technology Research Institute of Traditional Chinese Medicine, [f]Department of Orthopedic Surgery, Orthopedic Hospital of Guangzhou, [g]Department of Orthopaedics and Traumatology, The First Affiliated Hospital of Guangzhou University of Chinese Medicine, Guangzhou, [h]The 2nd Department of Arthrosis, Wangjing Hospital of China Academy of Chinese Medical Sciences, [i]School of Acupuncture-Moxibustion and Tuina, Beijing University of Chinese Medicine, Beijing, [j]Department of Rehabilitation, Kunming Municipal Hospital of Traditional Chinese Medicine, The Third Affiliated Hospital of Yunnan University of Chinese Medicine, Kunming, [k]Department of Orthopaedics, Nanchang Hongdu Hospital of Traditional Chinese Medicine, Nanchang, [l]Fifth Department of Orthopedics (Foot and Ankle Surgery), Shunde Hospital of Guangzhou University of Chinese Medicine, Foshan, [m]Emergency Department, Dongguan People's Hospital, Dongguan, People's Republic of China and [n]Department of Diabetes, Central Clinical School, Monash University, Melbourne, Victoria, Australia

Sponsorships or competing interests that may be relevant to content are disclosed at the end of this article.

**Corresponding author. Address: The First Affiliated Hospital of Guangzhou University of Chinese Medicine, NO.16 Jichang Road, Baiyun District, Guangzhou 510405, People's Republic of China. Tel.: +860 203 6488 481. E-mail: ainemylyy@163.com (Z. Jiang), and School of Acupuncture-Moxibustion and Tuina, Beijing University of Chinese Medicine, Liangxiang Campus of Beijing University of Chinese Medicine, Liangxiang Higher Education Park, Fangshan District, Beijing 102488, People's Republic of China. Tel.: +860 106 4287 525. E-mail: wxtong642@foxmail.com (X. Wang).*

International Journal of Surgery (2024) 110:3269–3284

Received 5 December 2023; Accepted 22 February 2024

Supplemental Digital Content is available for this article. Direct URL citations are provided in the HTML and PDF versions of this article on the journal's website, www.lww.com/international-journal-of-surgery.

Published online 19 March 2024

http://dx.doi.org/10.1097/JS9.0000000000001291

Introduction

Trauma, tumors, osteonecrosis, severe infections, and congenital deformities can cause segmental bone defects[1]. Typical clinical approaches utilized for the treatment of bone defects encompass various methods such as Ilizarov technique (also known as distraction osteogenesis)[2], Masquelet technique[3], free vascularized bone grafting[4], and tissue engineering[5]. The first three treatment approaches primarily employ 'bone-to-bone' fusion for managing segmental bone defects, but they have the disadvantage of a long postoperative treatment process[6]. Tissue engineering is an emerging approach for treating bone defects, and biomaterials employed for bone repair demand specific attributes, such as porous structures (micropores or macropores), biocompatibility, degradability, osteoinductivity, and malleability, and adequate biomechanical properties to facilitate tissue formation and inward growth (bone conduction)[7,8]. However, relying solely on biomaterials has not been successful in inducing significant bone formation. Therefore, biomaterials were often combined with bone morphogenetic protein (BMP) that activate bone induction signaling pathways, vascular endothelial growth factor (VEGF) that promotes angiogenesis, and pharmaceutical agents with vascular and osteoinductive properties. However, the utilization of BMP, especially in supraphysiological doses, can lead to increased formation of osteoclasts and premature bone resorption[9]. VEGF has similar effects to BMP2 in inducing bone formation and angiogenesis. However, the clinical application of these growth factors was hindered due to their inherent limitations, including instability and a brief duration of effectiveness[10]. Therefore, there is a growing interest in drugs that have both vascular and osteoinductive effects, which has become a focus of current bone tissue engineering[11]. For example, Li Limei *et al.* used a Hydroxyapatite (HA)-loaded scaffold with the herbal active ingredient gastrodin, which facilitated the transformation of proinflammatory macrophages (M1 phenotype) into anti-inflammatory and prohealing macrophages (M2 phenotype), accelerating vascular, and bone formation in a rat femoral condyle defect. This novel biomaterial with immunomodulatory properties presents a compelling strategy for the advancement of bone regeneration[12]. In the preliminary drug screening, we found that TFRD, a major active component of *Rhizoma Drynariae*, promoted the growth of rat tibial bone defects when administered orally[13], and was also shown to be effective in clinical trials[14]. However, preliminary experiments revealed that long-term oral administration of TFRD to rats caused malnutrition. In a clinical setting, patients' compliance may also decrease due to long-term medication, leading to a decrease in treatment efficacy. Inspired by the *Illustrated Classics of Materia Medica* record that *Rhizoma Drynariae* can be decocted and applied to local part to cure fracture. TFRD was the main ingredients of *Rhizoma Drynariae* after decoction, therefore, we designed a TFRD drug-loaded scaffold for local drug release to reduce malnutrition caused by gastrointestinal reactions and authenticate its practical worth pertaining to tibial segmental bone defects.

According to the design requirements of the biomaterial scaffold, natural biomaterials (chitosan), synthetic inorganic materials (hydroxyapatite), and polymer (polydopamine, PDA) are commonly used in the design of biomaterial scaffolds. Chitosan possesses notable merits, including exceptional biodegradability, compatibility with biological systems, absence of toxicity, and especially antibacterial properties, which are significant for reducing local infection in bone defects[15]. Carboxymethyl chitosan (CMCS) emerges as a widely utilized derivative of chitosan, effectively preserving its exceptional biological characteristics while augmenting its solubility in water, making it commonly used in biomaterial scaffold design[16]. HA has been found to have good biocompatibility and, in the bio-scaffold for drug-loaded bone defect repair, HA also acts as a temporary scaffold to promote bone regeneration[17]. Polydopamine has good biocompatibility and exhibits strong adhesion to various substrates through covalent and/or noncovalent interactions. It can be used to bind various drugs or nanoparticles to the surface and undergo degradation under acidic conditions for bio-scaffold preparation[18]. Previous studies have found that in the event of an injury, there is a rise in the pH level of the wound attributed to microvascular leakage, nearing the optimal pH range for bacterial infection (around 7.4)[19]. Consequently, there is a shift towards alkalinity, with the pH range typically ranging from 7.5 to 8.9, leading to inflammation and extending the duration required for wound healing[19]. Controlling infection, reducing the pH value to maintain weak alkaline environment can significantly increase the activity of osteoblasts and inhibit the activity of osteoclasts, thus providing favorable conditions for bone regeneration[20]. In view of the fact that this condition is very important for inducing bone growth and releasing drug-loaded scaffolds, it is expected to prepare HA/CMCS/PDA/TFRD scaffolds by using the infection control characteristics of CMCS, the mechanical support of HA, the bone promotion properties of TFRD and the polymerization and degradation effects of polydopamine, and to conduct cell experiments and preclinical applications to explore its potential value in the field of bone defects.

Many preclinical applications of biomaterials only evaluate their osteogenic or angiogenic functions on small local defects. From the perspective of clinical orthopedic surgeons, the value of these evaluations is highly limited because patients with small local bone defects often experience self-healing or achieve excellent clinical recovery by filling with autologous or allogeneic bone, rarely considering the use of biomaterials. On the contrary, segmental bone defect is a challenging problem for clinicians, which requires patients to have strong courage and patience to face long-term health issues. Therefore, we explore the preclinical application potential of the HA/CMCS/PDA/TFRD scaffold through a rat tibial segmental bone defect model.

Based on all these scientific questions, in this work, we attempt to develop a novel HA/CMCS/PDA/TFRD scaffold. The morphology of the scaffold was examined using both optical and electron microscopy techniques, while its composition was determined through X-ray diffraction (XRD) analysis.

HIGHLIGHTS

- Inspired by the local application of total flavonoids of *Rhizoma Drynariae* (TFRD) to cure fractures, a 3D-printed HA/CMCS/PDA/TFRD scaffold was designed.
- Cell experiments and preclinical applications were conducted to explore the potential application of HA/CMCS/PDA/TFRD scaffold in the field of segmental bone defects.
- TFRD-loaded biomaterial can reduce malnutrition caused by gastrointestinal reactions and maintain patient compliance.

Functional groups were determined by Fourier-transform infrared (FTIR) spectroscopy. The in vitro degradation, pH variation, and drug release performance of scaffold were evaluated using simulated body fluid. In vitro experiments involve culturing bone marrow mesenchymal stem cells (BMSCs) and human umbilical vein endothelial cells (HUVECs) with the scaffold extract. To examine the impact of the scaffold extract on the osteogenic differentiation of BMSCs, Alkaline Phosphatase (ALP), and Alizarin Red S (ARS) were performed, along with measurements of the expression levels of the Runx2, OCN, and BMP2 genes and proteins. To investigate the impact of the scaffold extract on the behavior of HUVECs, cell migration, tube formation assays, the mRNA and protein levels of PI3K, AKT, HIF-1α, and VEGF were evaluated. To evaluate the preclinical application potential of the scaffold, we selected a rat tibial segmental bone defect model. Biocompatibility evaluation was conducted by collecting blood samples from rats at postoperative days 1, 3, 7, and 14 to observe infection indicators, inflammation markers, and liver and kidney function. X-ray imaging, angiography, micro-CT analysis, and histological analysis, were used to observe and evaluate the new bone formation process and vascular regeneration. The expression of CD31 and BMP2 was analyzed by immunohistochemistry, and the protein levels of BMP2 and VEGF in the bone defect area were measured. The biomechanics of the regenerated tibial segment were evaluated to observe its maximum failure stress. In summary, we have demonstrated for the first time that the HA/CMCS/PDA/TFRD scaffold, with its infection resistance, and drug-loading capabilities, promotes angiogenesis and osteogenesis to facilitate the healing of segmental bone defects. This presents a promising approach for addressing segmental bone defects.

Methods

This study has been reported in accordance with the ARRIVE guidelines (Animals in Research: Reporting In Vivo Experiments)[21] (Supplemental Digital Content 1, http://links.lww.com/JS9/C202).

Manufacturing scaffolds using 3D printing

Previous studies have found that PDA, as a drug carrier, can stably load drugs when mixed with dopamine and then subjected to PDA self-polymerization reaction under physiological conditions[22,23]. It exhibits strong potential for drug delivery by releasing drugs under local acidic conditions after reaching the cells. Therefore, the 3D Bio-Printer (Regenovo Biotechnology Co., Ltd.) was used to manufacture HA/CMCS/PDA/TFRD scaffolds (TFRD scaffolds). First, HA powder was prepared using a hydrothermal method based on previous studies[24]. A mixture of 4 ml of ethanol, 9 ml of deionized water, and 0.3 ml of 25 wt% ammonia was stirred at 30°C for 0.5 h[25]. TFRD (final concentration of 0.125 mg/ml) and dopamine hydrochloride solution (1 ml, 0.03 g/ml) were added, and PDA underwent self-polymerization in an alkaline solution. The HA powder weighing 1.2 g was introduced and agitated for 5 min, followed by an additional 15 min of ultrasonic stirring at 30°C. Finally, CMCS (1 g, degree of deacetylation $\geq 90\%$, MW: $2.0–2.5 \times 10^5$, Huameko) was added and stirred for 2.5 h at 30°C. The mixture underwent heating to 60°C and continued to be stirred for a period of 0.5 h. The HA/CMCS/PDA/TFRD scaffold was printed with a 0.4 mm nozzle (machine air pressure 0.08–0.5 MPa, speed 12–18 mm/s, fiber spacing 0.6 mm, layer height 320 μm). The size of the scaffold was $4 \times 3 \times 3$ mm. A similar protocol was used to prepare Control scaffolds without TFRD. After printing, the scaffolds were crosslinked with a 0.5% solution of pyrogallic acid dye (purity $\geq 98\%$, Linyuan Zhixin Biotechnology) for 4 h, followed by three consecutive rinses with deionized water. Finally, the scaffolds were freeze-dried and sterilized by Co60 irradiation.

Characterization of the scaffolds

The macroscopic morphology of the prepared scaffolds was examined using an optical microscope (Olympus, GX51). After sputter coating with gold using a cold sputter coater (Scd005, Leica) at 5 kV, the scaffolds were subjected to characterization utilizing a scanning electron microscope (SEM, ZEISS). The mineral composition of the scaffolds was determined by conducting XRD analysis using a D/max-2200PC automatic diffractometer (Rigaku) over the 2θ range of 10° to 70°. The infrared (IR) spectra of the samples were obtained using an IR Prestige-21 spectrometer (Shimadzu) equipped with KBr pellets, covering the wavelength range of 400 to 4000 cm^{-1}.

In vitro degradation experiment

After adjusting the pH of the phosphate-buffered saline (PBS) to 7.4 through the utilization of NaOH and HCl solutions, the degradation experiment was conducted. A total of 40 mg of the scaffold was completely immersed in 2 ml of PBS in a centrifuge tube, sealed, and transferred to a THZ-D constant temperature oscillator (Suzhou Peiying Laboratory Equipment Co., Ltd.) set at 37°C and 80 rpm.

Degradation performance

At weeks 2, 4, 8, and 12, the scaffolds were carefully moved to fresh empty centrifuge tubes and subjected to three gentle rinses with ddH_2O. Subsequently, the samples were subjected to drying in a 37°C drying oven until a constant weight (W1) was achieved. The weight was measured using a German Sartorius Secura series electronic balance (Sartorius), and the PBS was renewed every week. Three scaffolds were used for the experiment.

$$WL = (W_0 - W_1/W_0) \times 100\% \quad (1)$$

Equation (1) was used to monitor the weight loss percentage (WL%) of the scaffold, where the initial weight of the scaffold was denoted as W0.

pH measurement

The Sartorius standard model PB-10 pH meter (Guangzhou Shouke Instrument Technology Co., Ltd.) was used to measure the pH values of the scaffolds completely immersed in PBS at different degradation times (weeks 2, 4, 8, and 12) following the instructions provided in the user manual (https://wenku.baidu.com/view/3166f9bc58f5f61fb6366602.html). The pH values were determined, and the corresponding change curves were plotted. A control group was included, consisting of PBS without the presence of scaffolds, and the PBS was not replaced during the experiment. Three bio-scaffolds were used for the experiment.

Drug release determination[26]

Before conducting in vitro drug release determination, the maximum absorption wavelength of the drug and a standard curve of drug concentration gradient were established. 100 mg of TFRD was dissolved in 2 ml of PBS. The beaker was placed in a THZ-D constant temperature oscillator (Suzhou Peiying Laboratory Equipment Co., Ltd.) set at 37°C and 80 rpm for complete dissolution for 2 h. Following a centrifugation step conducted at 4000 rpm for a duration of 12 min, the resulting supernatant was gathered. The maximum absorption wavelength was measured three times using a UVmini-1240 UV-visible spectrophotometer (model: UVmini-1240, SHIMADZU). The average value was determined to be 360 nm. Then, the absorbance values of different dilutions of the drug (0.05, 0.1, 0.2, 0.25, 0.5, 1.25, 2.5 mg/ml) were measured at a wavelength of 360 nm to construct a standard curve. Next, The scaffolds were submerged in PBS for various durations, including 1, 2, 4, 6, 8, 12, 24 h, as well as 2, 3, 4, 5, and 7 days. After removal, 200 μl of the solution was taken and the absorbance is measured at 360 nm. Then, 200 μl of PBS was added back to the sample. The absorbance of the drug in the scaffold was calculated by subtracting the absorbance of the control scaffold. A concentration release curve of the drug in the scaffold was plotted based on the absorbance values obtained.

Cell experiments

Preparation of scaffold extract

The preparation of scaffold extracts followed established procedures as described in the study by Wang *et al*.[27] By employing a mass/volume ratio of 200 mg/ml, immerse the scaffold powder in osteogenic medium (consisting of dexamethasone (100 nM, Sigma), β-glycerophosphate (10 mM, Sigma), DMEM, ascorbic acid (50 μg/ml, Sigma)) or endothelial cell basal medium (ECM, Sciencell) without serum. Following a 24 h incubation period at 37°C, then centrifuged and filtered the solution through a sterile 0.22 μm filter to acquire the scaffold extract.

Cell culture

BMSCs (CP-R131, Procell Life Science & Technology Co., Ltd.) and HUVECs (iCell-h110, iCell Bioscience Inc.) were cultured in α-MEM supplemented with 1% penicillin-streptomycin (*P*/S) and 10% fetal bovine serum (FBS) to promote their growth. The cells were cultivated in a controlled environment with 37°C temperature, 5% CO_2, and adequate humidity. The growth medium was refreshed every 72 h. Upon reaching an approximate confluency of 80%, the cells were subjected to passaging, and cells from passages three to five were employed for subsequent experimental analyses.

To investigate the effect of the scaffold extract on the osteogenic differentiation of BMSCs, the cells were cultured in osteogenic differentiation medium supplemented with 10% FBS and 1% *P*/S. In addition, used osteogenic differentiation medium supplemented with 5 ng/ml TGF-β, 10% FBS, and 1% *P*/S as a positive control. ALP and ARS assays were conducted to assess the impact of the scaffold extract on osteogenic differentiation. Quantification was conducted by randomly selecting five fields. The experiments were repeated three times.

In order to evaluate the influence of the scaffold extract on HUVECs behavior, the cells were cultured in endothelial cell basal medium extract (1001, ScienCell ECM) according to the product instructions, supplemented with 5% FBS, 1% *P*/S, and 1% Endothelial Cell Growth Supplement. Additionally, used complete endothelial cell culture medium with or without the addition of 10 μM PI3K inhibitor (LY294002) as a control. Cell migration and tube formation assays were conducted to assess the influence of the scaffold extract on HUVEC behavior. Quantification involved the random selection of five fields. All experiments were carried out in triplicate.

Cell counting Kit-8 (CCK-8) assay

The CCK-8 was used to determine the viability of HUVECs or BMSCs to assess the cytotoxicity of the scaffold extract culture medium. Cells were seeded in a 96-well plate at a density of 5000 cells per well, with 100 μl of culture medium. Following incubation for 24, 48, and 72 h, each well received 10 μl of CCK-8 solution (Ab228554, abcam). The plate was then incubated in a light-restricted setting at 37°C for 2 h. The absorbance was measured at 460 nm.

ALP

A total of 5×10^4 BMSCs were seeded per well in a 24-well plate and subsequently cultured in α-MEM medium supplemented with 1% *P*/S for a duration of 24 h at 37°C. Following that, the medium was substituted with different scaffold extracts, and the medium was refreshed every 72 h for a total of 14 days of cultivation. After 14 days, the cells were fixed with 4% paraformaldehyde (PFA) at room temperature for 30 minutes. ALP staining solution (C3206, Beyotime) was applied to the cells for staining purposes, and the staining process was carried out at room temperature in a dark environment for a duration of 30 min. Subsequently, the cells were subjected to three rounds of washing with 1× PBS, with each wash lasting for 5 min[28].

Alizarin red staining (ARS)

BMSCs were seeded in a 24-well plate at a density of 5×10^4 cells per well. Subsequently, the cells were cultured at 37°C in α-MEM medium supplemented with 1% *P*/S for a period of 24 h. The medium was substituted with different scaffold extracts, and the cells were cultured for 21 days. After fixation with a 4% PFA, the cells underwent triple washing with distilled water before being subjected to Alizarin red staining at a temperature of 37°C for 30 min. Following a subsequent rinse with distilled water, images were captured under a microscope[29].

Cell migration

The Transwell migration assay was employed to assess the migratory behavior of HUVECs in response to the scaffold extract[30]. In the upper chamber of a 24-well Transwell plate (with an 8 μm pore size, Corning, USA), 200 μl of HUVEC suspension containing 2×10^4 cells was carefully added. In the lower chamber, 500 μl of various extracts was introduced. Following 24 h of cell culture, the HUVECs adhered to the underside of the membrane were cautiously rinsed with PBS and subsequently fixed with a 4% PFA solution for a duration of 30 min. Next, the nonmigrated cells present on the upper surface of the membrane were carefully eliminated using a cotton swab, followed by staining with 1% crystal violet for 10 min. Random images were captured using an inverted microscope (IX51, OLYMPUS). The

results were compared to the control group, and the experiment was performed three times.

Tube formation assay

According to the previous research protocols[31], HUVECs (2×10^4 cells per well) were cultured in different scaffold extract for 12 h. The morphological changes of HUVECs were observed under a microscope to assess the in vitro angiogenic potential of the scaffold. In brief, a 96-well plate was coated with 50 μl of Matrigel (BD, USA) and incubated at a temperature of 37°C for a period of 30 minutes to form a gel. HUVECs were suspended in 100 μl of different scaffold extracts and incubated at 37°C with 5% CO_2 for 12 h. The average tube length was measured using ImageJ software.

Animal experimental modeling

Grouping

A total of 81 healthy adult male Sprague Dawley rats, weighing between 280–300 g, were included in the study. To ensure randomization, the rats were divided into three groups using a random number table method. The groups were as follows: the control group, which had a segmental tibial bone defect (Control Group); the group with segmental tibial bone defect implanted with a control scaffold without TFRD (Blank Biological Scaffold, BBS Group); and the group with segmental tibial bone defect implanted with a TFRD biological scaffold (TFRD Biological Scaffold, TBS Group).

Animal model construction and postoperative management

The construction of the tibial segmental bone defect with scaffold implantation model was similar to previous bone defect models[31]. However, to reduce the risk of infection and shorten the modeling time, rats were first subjected to external fixation after anesthesia to stabilize the tibia. A 4 mm segmental bone defect was created in the midshaft of the tibia and a scaffold was implanted. Simultaneously, a segmental bone defect was established as the control group. Postoperatively, analgesic medication was administered to alleviate pain.

Biocompatibility assessment

To evaluate the in vivo safety of the scaffold, biocompatibility evaluations were performed. Blood samples were collected from three rats in each group at postoperative days 1, 3, 7, and 14. The GRT-6000 hematology analyzer (Jinan Greetech Technology Co., Ltd.) was used to measure white blood cell count (WBC), percentage of neutrophils (NEU%), and platelet count (PLT) to assess the rats' infection status. To assess the inflammatory response in the rats, Enzyme-linked immunosorbent assay (ELISA) kits (BioLegend) were employed for the quantification of interleukin 1 (IL-1), tumor necrosis factor-alpha (TNF-a), and interleukin 6 (IL-6) levels. The Roche Cobas 8000 fully automated biochemical analyzer (Roche Diagnostic Products (Shanghai) Co., Ltd.) was used to measure serum alanine aminotransferase (ALT), albumin (ALB), aspartate aminotransferase (AST), creatinine (Cre), serum urea nitrogen (Urea), and phosphorus (P) to assess the rats' liver and kidney function. For each time point, three rats were selected from each group for measurement.

X-ray, angiography, and micro-CT analysis

Continuous X-ray images were obtained using an X-ray machine (ZU-L5TYH, Hitachi Medical Systems Suzhou Co., Ltd.) at postoperative weeks 4, 8, and 12 to visualize the dynamic process of bone healing. The Lane-Sandhu X-ray scoring system was used to evaluate the osteogenic effect of the tibial bone defect in rats at 12 weeks postoperatively, assessing bone formation, bone bridging, and bone remodeling dimensions[32]. Euthanasia was performed on rats at 12 weeks postoperatively, followed by perfusion with Microfil (Microfil MV-0, Flow Tech;) to visualize the blood vessels. In brief, after anesthesia, the chest cavity was opened, exposing the aorta, and the right atrial appendage was incised. Subsequently, the vascular system was flushed with sterile physiological saline containing 4 U/ml sodium heparin, and the tissues were fixed with 4% PFA. After rinsing with NaCl to remove the excess PFA, the tissues were perfused with Microfil. The samples were kept at a temperature of 4°C overnight to facilitate the polymerization of the contrast agent. The tibia was carefully dissected and subsequently immersed in a 4% PFA solution for a duration of 48 h for fixation. and then micro-CT imaging was used to measure the tissue mineral density (TMD, also called bone mineral density) and bone volume/tissue volume (BV/TV) of the defect area. Following decalcification using a 10% ethylenediaminetetraacetic acid (EDTA, 183004, Wuhan Servicebio Technology Co., Ltd), micro-CT was used to visualize the vascular volume surrounding the bone defect area. The parameters were set as follows: Resolution of 9 um, energy utilization of 80 kV, 100 uA; The rotation angle for each scan is 0.6°, with a total rotation of 180° for scanning. Three rats were selected for measurement in each group.

Tissue morphology assessment and immunohistochemistry

Rat liver and kidney tissues at postoperative days 1, 3, 7, and 14, as well as decalcified tibial samples from rats at 12 weeks postoperatively, were dehydrated using an ethanol gradient and embedded in paraffin. Subsequently, coronal sections were prepared for the liver and kidney tissues, whereas sagittal sections were prepared for the bone tissues, all with a uniform thickness of 5 μm. H&E staining was performed on the liver and kidney tissues, while the bone tissues underwent staining with H&E, Masson's trichrome, and Safranin O.

Immunohistochemical staining for BMP2 and CD31 was conducted to assess the expression of osteogenic and vascular-related proteins. In brief, paraffin-embedded sections underwent deparaffinization, rehydration, and antigen retrieval. The sections were subjected to an overnight incubation at 4°C with primary antibodies, including rabbit anti-BMP2 (ab284387, 1:100, Abcam) and anti-CD31 (ab222783, 1:100, Abcam). Following this, the sections were incubated with secondary antibodies conjugated with horseradish peroxidase (HRP) (Santa Cruz Biotechnology). Finally, counterstaining was performed using hematoxylin. Tissue images were captured, and the Image-Pro Plus software (version 6.0, Media Cybernetics) was employed to analyze the area of positive staining within five randomly selected regions of the bone regeneration area. Three rats were selected for measurement in each group.

Real-time qPCR

Total RNA was extracted using a kit (Takara). The concentration and purity of the RNA were assessed using the NanoDrop 2000. The PrimeScript RT kit (Takara) was used for reverse transcription of the RNA, followed by quantitative PCR (qPCR) using Premix Ex Taq II. The cycling conditions were as follows: 30 s at 95°C, followed by 40 cycles of 5 s at 95°C and 30 s at 60°C. The expression levels of the target genes were standardized by normalizing them to the reference gene GAPDH. The qRT-PCR results were analyzed using the $2^{-\Delta\Delta CT}$ method. The primer sequences used in qRT-PCR were shown in Table S1 (Supplemental Digital Content 2, http://links.lww.com/JS9/C203). Three rats were selected for measurement in each group.

Western blot analysis

Cells or bone tissue powder obtained by liquid nitrogen grinding were added to a lysis buffer comprising inhibitors for proteases and phosphatases. And then place on ice for 10 min, followed by centrifugation at 12 000 rpm for 10 min. The supernatant was collected, and the protein concentration was determined using a BCA protein quantification kit (AS1086, Wuhan Aisbiotech Co., Ltd.). Protein denaturation was performed, and samples were loaded onto SDS-polyacrylamide gel for total protein separation, followed by transfer onto a polyvinylidene fluoride (PVDF) membrane. After blocking the membrane with 5% skimmed milk at room temperature for 1 h, the indicated primary antibodies were applied and left to incubate overnight at 4°C, including Runt-related transcription factor 2 (Runx2, ab236639, 1:1000), BMP receptor type 2 (BMP2, ab130206, 1:1000), Osteocalcin (OCN, DF12303, 1:1000), anti-PI3K (#4257, 1:1000), p-PI3K (#4228, 1 : 1000), Phospho-Akt (p-AKT, 1:1000), anti-AKT (AF0045; 1:1000), anti-GAPDH (#2118, 1:1000), anti-HIF-1α (#14179, 1:1000), and anti-VEGFA (ab214424, 1:1000). The PVDF membrane was subjected to incubation with secondary antibodies conjugated with HRP at room temperature. The antigen-antibody complexes were visualized using an enhanced chemiluminescence reagent (MeiLun Biotech). Image quantification was performed based on the grayscale values of the bands. Three rats were selected for measurement in each group.

Biomechanical test

The regenerated tibial segment was extracted and ground into a segment of ~4 × 3 × 3 mm in size to evaluate the maximum failure stress of the regenerated tibia at 6 months postoperatively. The biological sample was placed between two rigid plates mounted on an electronic universal testing machine (Model 6800, Instron). Compressive loads were applied at a constant displacement rate of 1 mm/min until the bone sample failed, and load and displacement data were collected. Simultaneously, healthy corresponding segment tibial specimens were also measured. Three rats were selected for measurement in each group.

Statistical analysis

The data were subjected to normality testing using IBM SPSS Statistics version 26. For data that passed the normality test, the mean ± SD was used for representation. For data that passed the normality test and exhibited homogeneity of variance, one-way analysis of variance (ANOVA) was used. In cases of heterogeneity of variance, Dunnett's T3 test was employed. For repeated measures data, repeated measures ANOVA was used. Nonparametric tests were used for data that did not pass the normality test (Lane-Sandhu X-ray scores). A *P*-value lower than 0.05 was considered statistically significant. GraphPad Prism (version 9.0, USA) was used to generate the figures.

Results

The scaffold containing TFRD exhibits porosity, good degradation performance, and drug release properties

The 3D printed HA/CMCS/PDA/TFRD scaffold was successfully designed and prepared, and its characterization and in vitro degradation performance were further evaluated (Fig. 1A). The macroscopic and microscopic structures of the scaffold were shown in Figure 1B. Macroscopically, the HA/CMCS/PDA/TFRD scaffold had a cylindrical shape. Under the microscope, it was observed that the scaffold slightly shrinks and the surface becomes rough, uneven, and even has some cracks after cross-linking and freeze-drying. The majority of the pore sizes were around 600–800 μm. The interconnected pores within the scaffold support cell growth and proliferation. SEM micrographs showed that the printed porous structure has a uniform and controlled architecture, with white protrusions formed due to the addition of HA particles.

To characterize the scaffold's crystal phase and composition, XRD and infrared spectroscopy were performed. From the XRD pattern (Fig. 1C), the peak positions and intensities correspond to those of crystalline HA. The characteristic peaks were observed at 10.820°, corresponding to the crystal plane (1 0 0); 25.879°, corresponding to the crystal plane (0 0 2); 31.773°, corresponding to the crystal plane (2 1 1); 39.818°, corresponding to the crystal plane (3 1 0); 46.711°, corresponding to the crystal plane (2 2 2); 49.468°, corresponding to the crystal plane (2 1 3); and 53.143°, corresponding to the crystal plane (0 0 4). This indicates that the HA in the scaffold exhibits good crystallinity without significant impurities.

In the FTIR spectrum (Fig. 1D), the characteristic peaks of CMCS mainly originate from the stretching vibrations of -NH and -OH groups (3350 cm^{-1}), the CH2 groups (2925 cm^{-1}), the asymmetric (1591 cm^{-1}) and symmetric (1423 cm^{-1}) stretching vibrations of carboxyl groups, the coupling of N-H bending and C-N stretching vibrations resulting in the amide band (1331 cm^{-1}), and the stretching vibrations of C-O bonds (1034 cm^{-1}). After the addition of TFRD, the scaffold containing TFRD exhibits all the characteristic peaks of CMCS, while the characteristic peaks of TFRD mainly arise from the C-O bonds (849 cm^{-1} and 1097 cm^{-1}) within the six-membered cyclic ether and the carbonyl group (1738 cm^{-1}). Additionally, due to the low content of PDA in the scaffold, there are no characteristic peaks of PDA observed in the FTIR spectrum. This indicates that the scaffold is primarily composed of CMCS and can load TFRD.

The in vitro degradation of the scaffold was presented in Figure 1E–G. In terms of pH variation, at 12 weeks, the scaffold containing TFRD exhibits a lower pH value compared to the PBS solution without the scaffold (Control group) (7.00 ± 0.13 vs 7.25 ± 0.06, $P = 0.04$), but no significant difference was observed compared to the scaffold without TFRD (Biological Scaffold group) (7.00 ± 0.13 vs 7.12 ± 0.06, $P = 0.21$). Regarding degradation performance, the scaffold containing TFRD was similar to the one without TFRD ($P > 0.05$). In terms of drug release, the

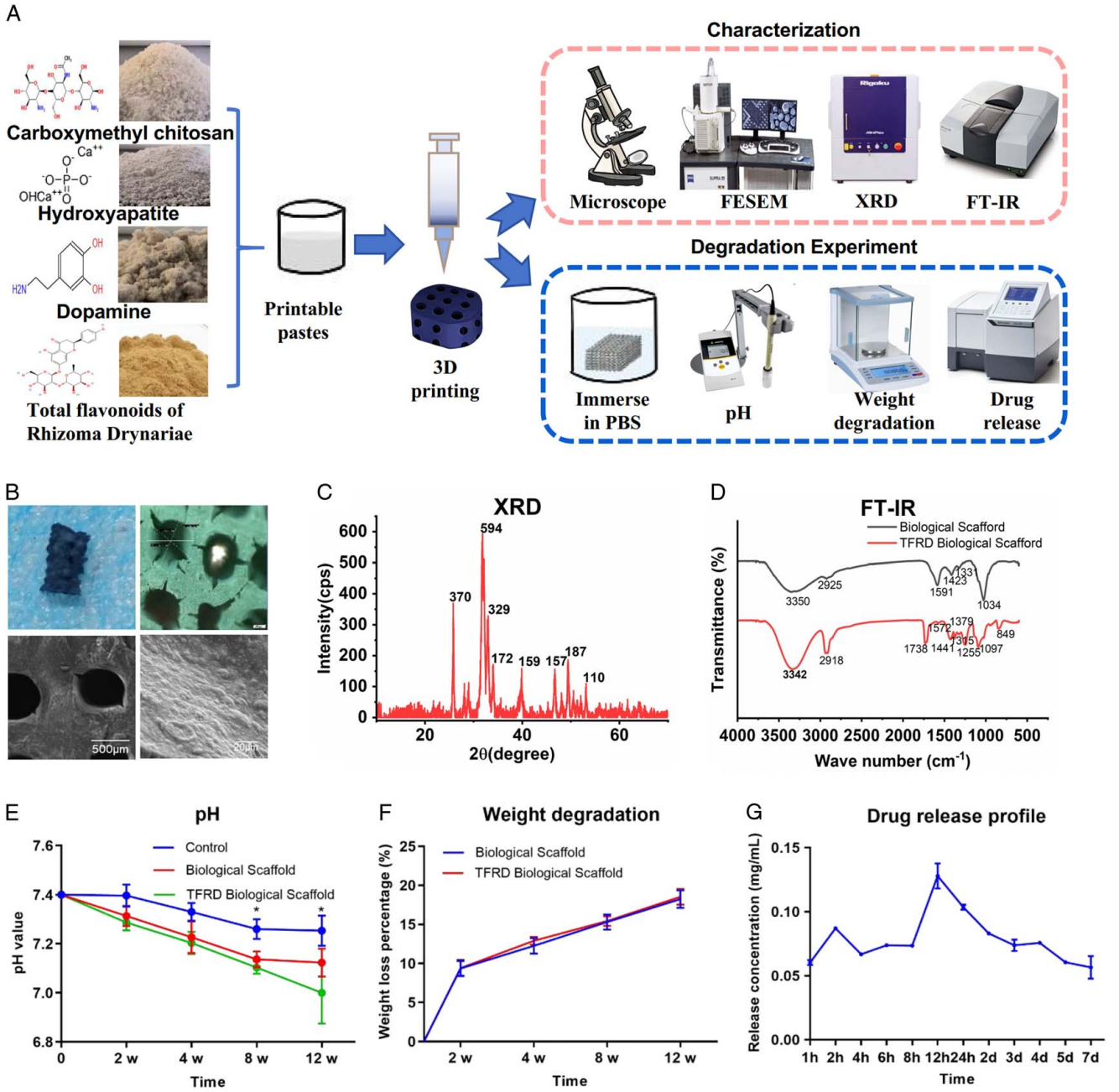

Figure 1. Preparation, characterization, degradation performance, and drug release performance of HA/CMCS/PDA/TFRD Scaffold. (A) Preparation, characterization, and degradation performance evaluation of HA/CMCS/PDA/TFRD scaffold. (B) Macro view and micro view and SEM results of the scaffold. (C) XRD spectrum of the scaffold. (D) FTIR spectrum. (E) pH variation of scaffold immersed in PBS. (F) Degradation performance of the scaffolds. (G) Drug release performance of HA/CMCS/PDA/TFRD scaffold. $N = 3$, $^*P < 0.05$.)

release of the drug from the drug-loaded scaffold fluctuates, reaching a peak at 12 h and then slowly decreasing, maintaining a relatively stable level.

In vitro osteogenic differentiation of BMSCs promoted by scaffold extraction

Figure 2A illustrates the preparation of scaffold extracts by immersing the scaffold powder in serum-free osteogenic medium. The cytotoxicity of the scaffold extracts on BMSCs was evaluated using CCK-8 assay, while ALP and ARS assays were conducted to investigate the effect of the scaffold extracts on BMSCs osteogenic differentiation. PCR and WB analyses were performed to examine the expression of osteogenic-related genes and proteins (OCN, BMP2, Runx2). To assess the influence of the scaffold on cell proliferation, rat BMSCs were cultured with the scaffold extracts. The cell proliferation was compared among different scaffold extracts at 24, 48, and 72 h (Fig. 2B). For all extracts, the proliferation of BMSCs showed a positive correlation with the

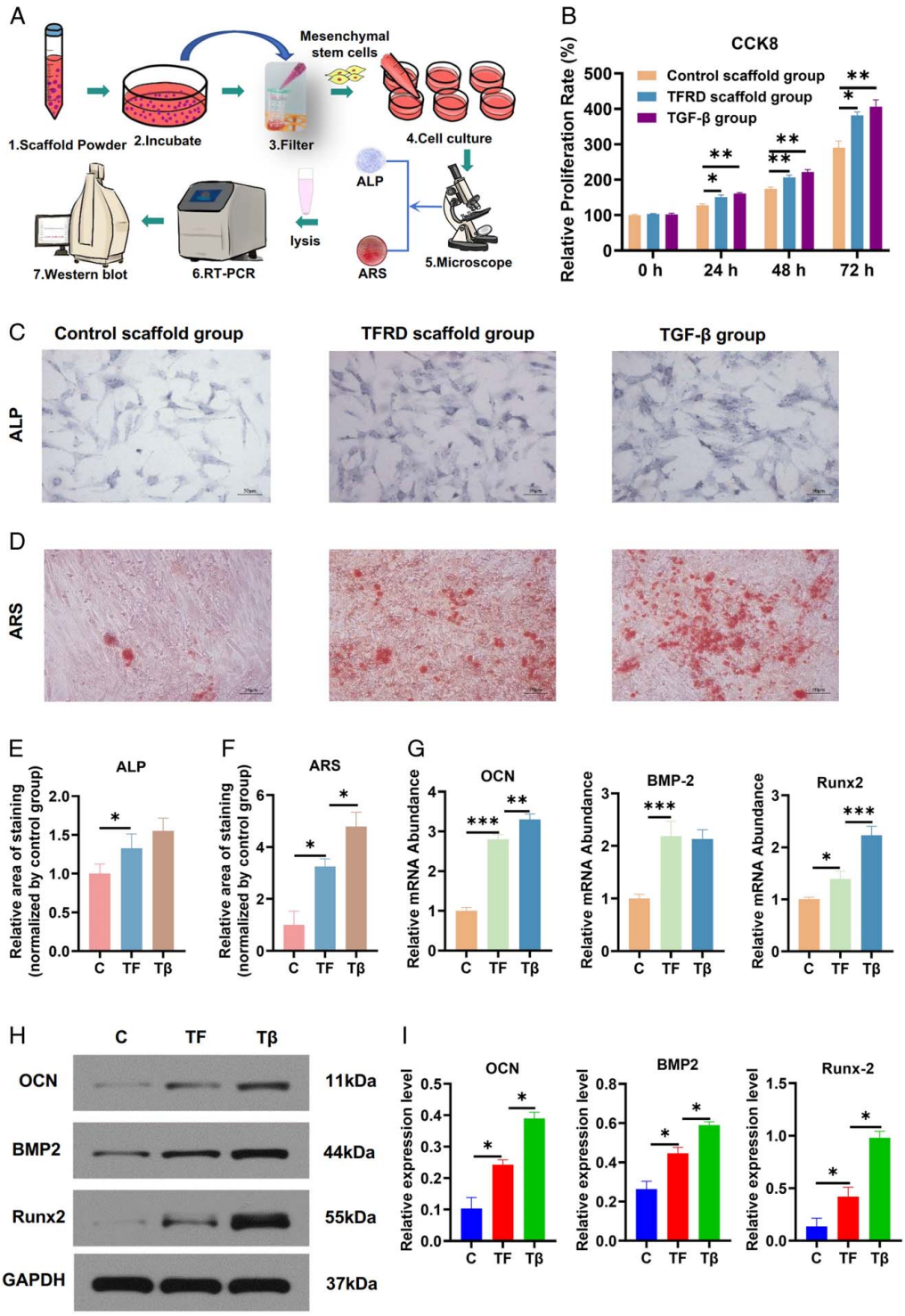

Figure 2. In vitro promotion of osteogenic differentiation of BMSCs by scaffold extracts. (A) Preparation of scaffold extracts by immersing the scaffold powder in serum-free osteogenic medium. CCK-8 assay was used to evaluate the cytotoxicity of the scaffold extracts on BMSCs, while ALP and ARS assays were conducted to investigate the effect of the scaffold extracts on BMSCs osteogenic differentiation. PCR and WB analyses were performed to examine the expression of osteogenic-related genes and proteins. (B) CCK-8 assay was used to assess the toxicity of the scaffold extracts on BMSCs. (C, E) ALP staining and relative activity of BMSCs cultured in the scaffold extracts for 14 days (scale bar = 50 μm). (D, F) ARS staining and relative staining intensity of BMSCs cultured in the scaffold extracts for 21 days (scale bar = 50 μm). (G) Impact of different scaffold extracts on the gene expression of Runx2, OCN, and BMP2 during BMSCs osteogenic differentiation. (H, I) Influence of different scaffold extracts on the protein expression of Runx2, OCN, and BMP2 during BMSC osteogenic differentiation, normalized to GAPDH. C, control scaffold group; TF, TFRD scaffold group; Tβ, TGF-β group. $N = 3$, $^{*}P < 0.05$, $^{**}P < 0.01$, $^{***}P < 0.001$.

culture time, indicating good cell viability. Interestingly, from 24 to 72 h, the proliferation of BMSCs in the TFRD scaffold group and TGF-β group was significantly higher than that in the control scaffold group ($P < 0.05$).

The ALP activity of BMSCs was measured 14 days after seeding the cells into the scaffold extract (Fig. 2C, E). The level of ALP expressed by cells on the scaffold extract containing TFRD was significantly higher than that of the blank scaffold extract group, and the level of ALP expressed by cells in the TGF-β group was higher than that of the scaffold extract group containing TFRD ($P < 0.05$). The positive staining of ARS was used to measure the mineralization of BMSCs in different scaffold extracts, as shown in Figure 2D, F. After 21 days of incubation with different scaffold extracts, although no significant difference in BMSCs mineralization was observed between the TFRD scaffold group and the TGF-β group, the staining intensity of the TFRD scaffold group was higher than that of the control scaffold group, indicating the osteogenic differentiation of BMSCs. To further investigate the effects of different scaffold extracts on the osteogenic differentiation of BMSCs, the expression of OCN, BMP2, and Runx2 genes and proteins was examined (Fig. 2G–I). After 21 days of incubation with different scaffold extracts, the TFRD scaffold group could enhance the expression levels of Runx2, OCN, and BMP2 genes and proteins, but this effect was still lower than the TGF-β group.

Promotion of angiogenic differentiation of HUVECs by scaffold extracts in vitro

Figure 3A illustrates the preparation of scaffold extracts by immersing the scaffold powder in endothelial cell culture medium. CCK-8 assay was conducted to assess the cytotoxicity of the scaffold extracts on HUVECs. Cell migration and tube formation assays were conducted to assess the effect of the scaffold extracts on angiogenic differentiation of HUVECs. PCR and WB analyses were performed to examine the expression of angiogenesis-related genes and proteins (PI3K, AKT, HIF-1a, VEGF). Complete culture medium with the addition of a PI3K inhibitor (LY294002) served as the control.

HUVECs were tested for the cytotoxicity of the scaffold extracts (Fig. 3B). The cell proliferation of HUVECs among different scaffold extracts at 24, 48, and 72 h showed a positive correlation with the culture time, indicating good cell viability. Importantly, from 24 to 72 h, the proliferation of HUVECs in the TFRD scaffold group was higher than that in the control scaffold group ($P < 0.05$).

During the early stage of blood vessel formation, directed migration of endothelial cells plays a crucial role. Cell migration of HUVECs was measured 24 h after seeding them in the scaffold extracts (Fig. 3C, D). Transwell experiments observed that the TFRD scaffold promoted HUVEC cell migration compared to the control scaffold group. Tube formation was a characteristic of HUVECs and reflects their ability for in vitro angiogenesis (Fig. 3C, E). After 12 h of culture, the TFRD scaffold showed a significant increase in the average tube length compared to the control scaffold group ($P < 0.05$). Angiogenesis-related factors such as PI3K, AKT, HIF-1a, and VEGF demonstrated an upregulation trend at the mRNA level (Fig. 3F–I), and p-PI3K/PI3K, p-AKT/AKT, HIF-1a, VEGF protein levels were elevated (Fig. 3J, K) after treatment with the TFRD scaffold extracts. The cell migration and tube formation effect were significantly inhibited when supplemented with the PI3K inhibitor, and the expression of angiogenesis-related genes and proteins showed a downregulation trend. In summary, these data confirm that the TFRD scaffold extract has the ability to enhance tube formation in HUVECs, possibly through upregulation of the PI3K/AKT/HIF-1a signaling pathway.

Biocompatibility testing

After anesthesia of rats, a segmental bone defect model was constructed in the tibial region. Blood samples were collected from rats at different times (1, 3, 7, 14 days) to examine infection and inflammation, liver and kidney function, and paraffin sections were used to assess liver and kidney conditions (Fig. 4A). The modeling process of the segmental bone defect in rat tibia was shown in Figure 4B. Throughout the study, no deaths or abnormal behaviors were observed in rats, indicating the absence of systemic toxicity from the implanted scaffold. Animal biocompatibility testing (Fig. 4C) found that the changes in infection and inflammation markers (WBC, NEU%, PLT, IL-1, IL-6, TNF-α), liver function (AST, ALT, ALB), and kidney function (Cre, UREA, P) in the Control Group, BBS Group, and TBS Group were consistent at postoperative days 1, 3, 7, and 14. Due to the addition of anti-infection drugs during the construction process, the BBS Group showed lower levels than the Control Group in terms of WBC, PLT, IL-1, and IL-6 (3d and 7d WBC: $P < 0.05$; 1d, 3d, 7d, 14d PLT: $P < 0.05$; 1d, 3d, 7d IL-1: $P < 0.05$; 1d and 3d IL-6: $P < 0.05$). Additionally, the TBS Group exhibited better anti-inflammatory effects than the BBS Group (3d and 14d WBC: $P < 0.05$; 1d, 3d, 7d PLT: $P < 0.05$; 1d, 3d, 7d, and 14d IL-1: $P < 0.05$; 1d, 3d, 7d, and 14d IL-6: $P < 0.05$). Elevated AST levels on the first day after surgery were considered to be caused by anesthesia. H&E staining showed no adverse inflammatory reactions in the liver and kidney of all groups (Fig. 4D), indicating the biocompatibility of the scaffold with no liver or kidney toxicity.

Scaffold-enhanced in vivo bone repair and vascular formation

Based on in vitro studies, we further evaluated the performance of HA/CMCS/PDA/TFRD in preclinical research. Male Sprague-Dawley rats were implanted with scaffolds in the tibial bone defect sites for 12 weeks. X-rays were performed at weeks 4, 8, and 12, and at week 12, samples were taken for CT scanning, histological analysis, immunohistochemical analysis, and WB analysis to observe bone repair and vascular formation (Fig. 5A). Throughout the study, no signs of necrosis were observed in rats with or without TFRD-containing scaffolds.

X-ray images and Lane-Sandhu X-ray scores of rats at different time points were shown in Figure 5B, C. At 4w and 8w, there were no significant differences in X-ray images among the Control, BBS, and TBS Group. After 12 weeks, both the TBS Group and BBS Group demonstrated substantial bone mineralization. Interestingly, no significant difference in Lane-Sandhu X-ray scores ($P > 0.05$) was observed between the two groups. However, it is worth noting that the TBS Group exhibited superior outcomes compared to the Control Group ($P < 0.05$).

The Micro-CT results of rats at 12 weeks were shown in Figure 5D–F. Following a treatment period of 12 weeks, the bone mineralization of rats in both the BBS Group and TBS Group exhibited comparatively superior outcomes compared to the

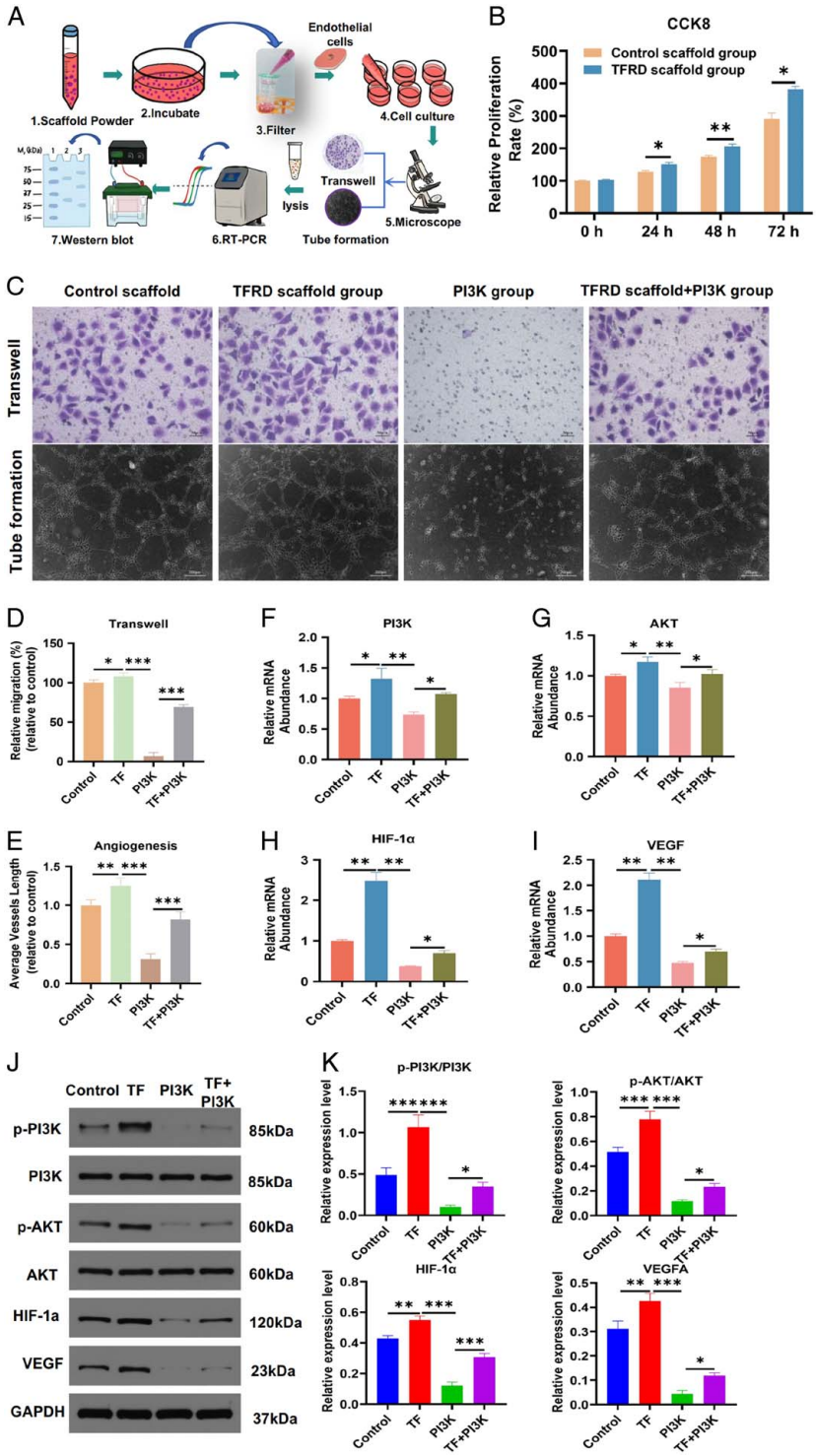

Figure 3. Promotion of angiogenic differentiation of HUVECs by scaffold extracts in vitro. (A) Preparation of scaffold extracts by immersing the scaffold powder in endothelial cell culture medium. CCK-8 assay was used to evaluate the cytotoxicity of the scaffold extracts on HUVECs. Cell migration and tube formation assays were conducted to investigate the effect of the scaffold extracts on angiogenic differentiation of HUVECs. PCR and WB analyses were performed to examine the expression of angiogenesis-related genes and proteins (PI3K, AKT, HIF-1α, VEGF). Complete culture medium with the addition of a PI3K inhibitor (LY294002) served as the control. (B) CCK-8 assay. (C) Transwell assay and tube formation assay (scale bar = 50 μm). (D) Relative migration rate in the Transwell assay. (E) Quantitative analysis of tube formation assay: relative average tube length. (F–I) Reverse transcription PCR analysis of (F) PI3K, (G) AKT, (H) HIF-1α, (I) VEGF mRNA in cells cultured with different scaffold extraction fluids. (J, K) WB analysis of PI3K, p-PI3K, AKT, p-AKT, HIF-1α, VEGF in cells cultured with different scaffold extracts, normalized to GAPDH. TF, TFRD scaffold group. $N = 3$, $^{*}P < 0.05$, $^{**}P < 0.01$, $^{***}P < 0.001$.

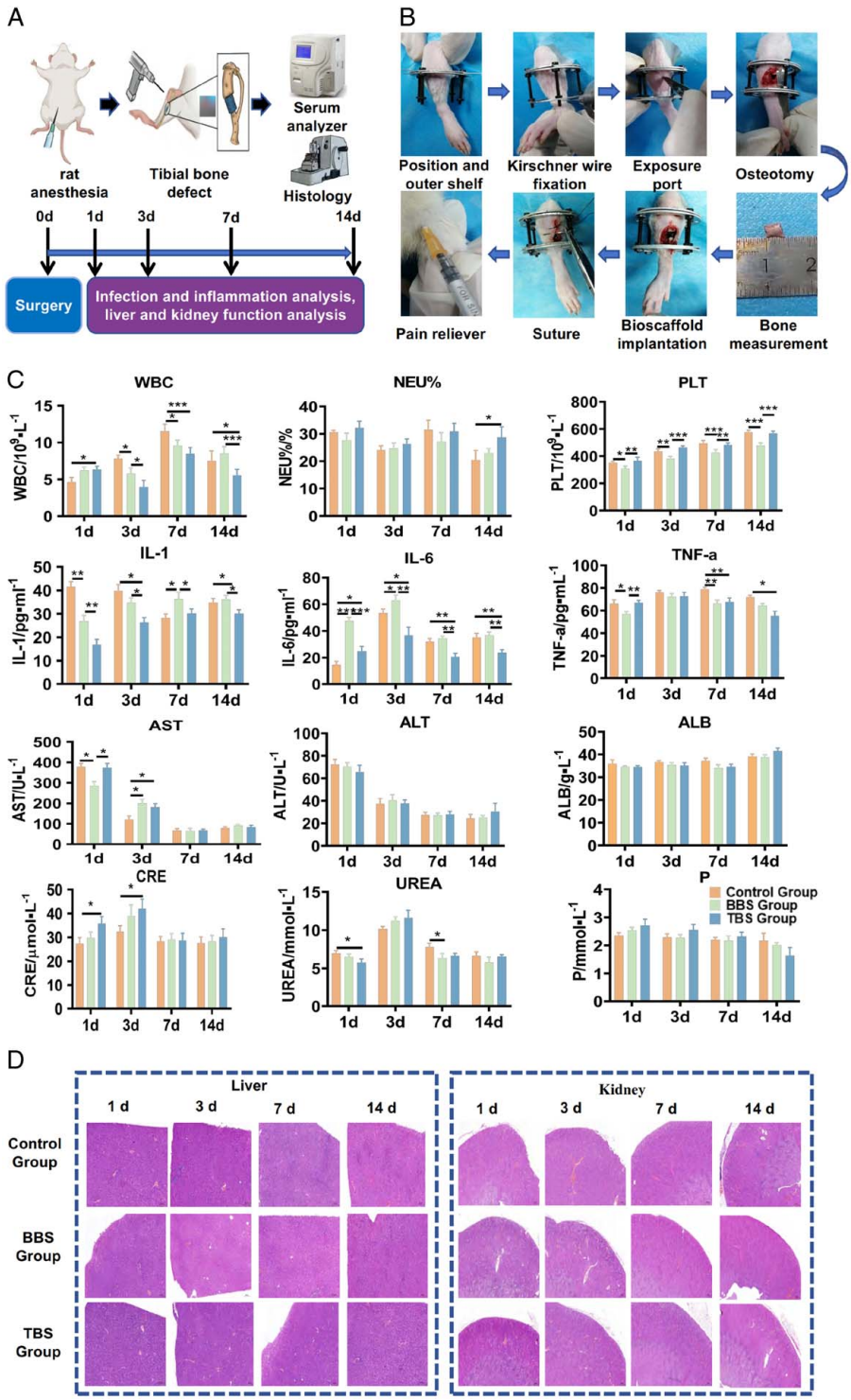

Figure 4. Construction of the implantation model of the scaffold in the bone defect and its biocompatibility evaluation. (A) After anesthesia of rats, a segmental bone defect model was constructed in the tibial region. (B) Blood samples were collected from rats at different times (1, 3, 7, 14 days) to examine infection and inflammation, liver and kidney function, and paraffin sections were used to assess liver and kidney conditions. (4) Modeling process of the segmental bone defect in rat tibia. (C) Blood tests of rats on postoperative days 1, 3, 7, 14 to measure infection markers (WBC, NEU%, PLT), inflammation markers (IL-1, IL-6, TNF-α), liver function (AST, ALT, ALB), and kidney function (Cre, UREA, P). (D) Liver and kidney sections of rats on postoperative days 1, 3, 7, 14 (40×). BBS Group, Blank Biological Scaffold; TBS Group, TFRD Biological Scaffold. $N = 3$, $^{*}P < 0.05$, $^{**}P < 0.01$, $^{***}P < 0.001$.

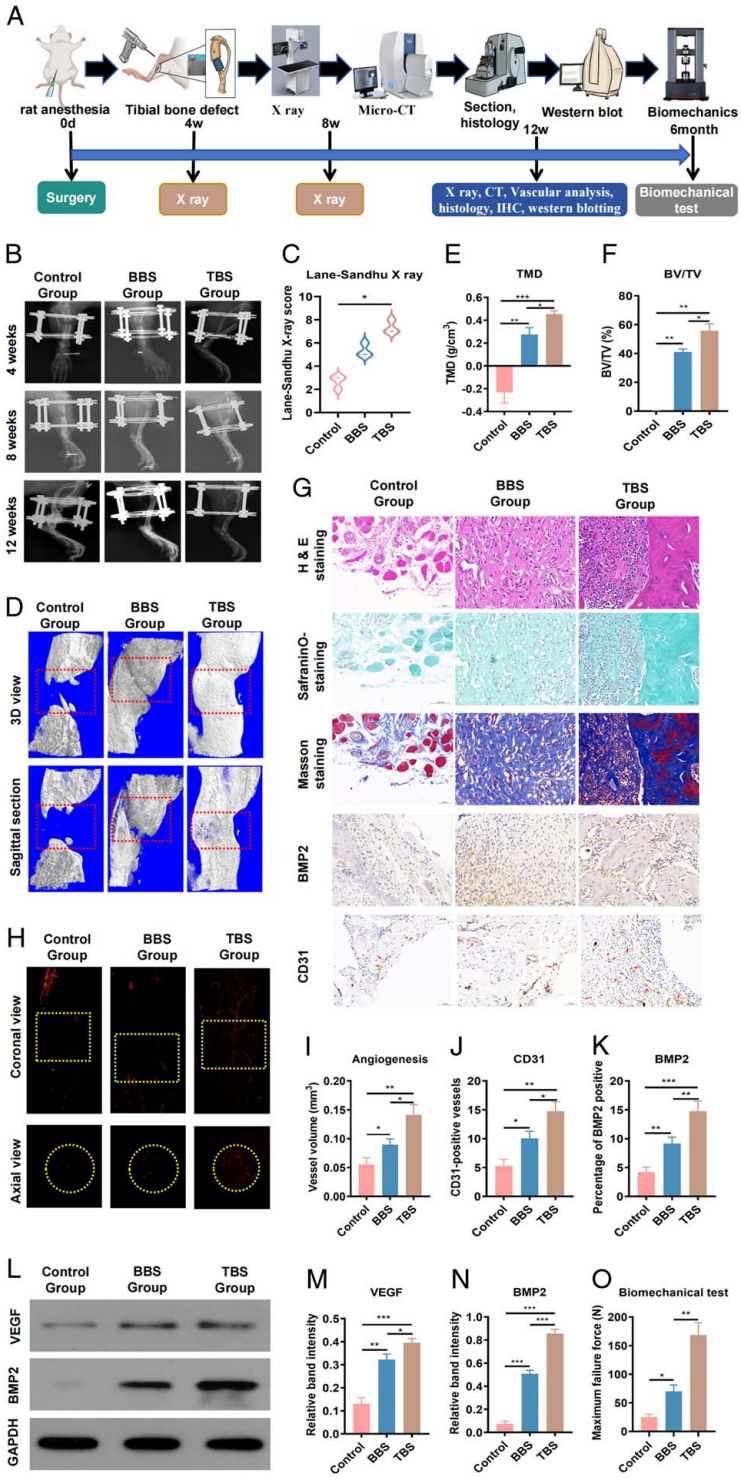

Figure 5. Enhanced bone repair and vascular formation with TFRD scaffold. (A) Male Sprague-Dawley rats were implanted with scaffold at the tibial bone defect site for 12 weeks. X-ray images of the rats were taken at weeks 4, 8, and 12, and at week 12, samples were collected for CT scanning, histological analysis, immunohistochemistry, and WB analysis to observe bone repair and vascular formation. Biomechanical tests were performed in the new bone tissue at 6 months postoperatively. (B) Tibial X-ray images of rats at weeks 4, 8, and 12 after surgery. (C) Lane-Sandhu X-ray scores at 12 weeks postoperatively. (D) 3D reconstruction and coronal section images of rat tibiae by Micro-CT at 12 weeks postoperatively, with gray to white representing poor to excellent bone mineralization. (E) TMD results. (F) BV/TV results. (G) Histological analysis (HE staining, SafraninO staining, and Masson's staining) and immunohistochemistry analysis (BMP2 and CD31) of newly formed bone tissue at 12 weeks postoperatively. Red arrows: Positive cells. (J, K) Quantification of positive cell count. (H) Coronal and transverse vascular angiography images of rat tibiae, with the yellow dashed lines indicating the region of interest (ROI). (I) Quantification of vascular volume in the bone defect area. (L-N) WB results and relative grayscale values of newly formed bone tissue in the rat bone defect area. (O) Biomechanical testing of new bone tissue in the tibial defect area of rats. The maximum failure force of the tibia of normal healthy rats was 660.23 ± 100.13N. Data were presented as mean ± SD. BBS Group, Blank Biological Scaffold; TBS Group, TFRD-loaded Biological Scaffold. $N = 3$, $^{*}P < 0.05$; $^{**}P < 0.01$.

Control Group (Fig. 5D). This result was also validated by bone microstructural parameters (Fig. 5E, F). The BBS Group and TBS Group exhibited significantly higher values in terms of TMD (0.28 ± 0.06 vs -0.23 ± 0.09; 0.45 ± 0.03 vs -0.23 ± 0.09) and BV/TV (41.00 ± 2.12 vs 0.43 ± 0.12; 55.82 ± 4.75 vs 0.43 ± 0.12) compared to the Control Group ($P < 0.05$). Furthermore, the TBS Group demonstrated superior TMD and BV/TV values compared to the BBS Group ($P < 0.05$). Immunohistochemical analysis revealed a significant enhancement in the expression of BMP2 in the bone defect area of both the BBS Group and TBS Group when compared to the Control Group (9.17 ± 1.10 vs 4.2 ± 0.85, 14.77 ± 1.72 vs 4.2 ± 0.85, $P < 0.05$). Additionally, the TBS Group displayed a higher expression of BMP2 compared to the BBS Group ($P < 0.05$) (Fig. 5H–J).

CD31 positive expression was distributed in the cytoplasm of endothelial cells and appears as brownish-yellow or brownish-brown color. Analysis of vascular angiography (Fig. 5H, I) demonstrated that the BBS Group and TBS Group exhibited higher numbers of blood vessels at the edges of the bone defect in comparison to the Control Group (0.09 ± 0.01 vs 0.06 ± 0.01, 0.14 ± 0.02 vs 0.06 ± 0.01). Notably, the TBS Group displayed a more pronounced induction of vascular formation compared to the BBS Group ($P < 0.05$). These findings were further corroborated by the immunohistochemical analysis of CD31 expression, which also demonstrated the same phenomenon (Fig. 5G, K). In the TBS Group, the expression of CD31 was observed to be greater compared to the BBS Group (14.75 ± 1.63 vs 10.06 ± 1.21, $P < 0.05$). Moreover, the BBS Group exhibited a higher expression of CD31 compared to the Control Group (10.06 ± 1.21 vs 5.28 ± 1.14, $P < 0.05$).

The bone formation at the site of scaffold implantation was shown in Figure 5G. HE staining showed that the TBS Group had higher levels of bone mineralization and evident mature bone tissue compared to the Control Group and BBS Group. SafraninO staining results revealed that both the control group and BBS group exhibited a significant amount of immature bone-like tissue, indicating incomplete restoration of the newly formed bone to its natural state. In contrast, the TBS group exhibited a greater presence of mature bone tissue within the bone defect area, surpassing both the control group and BBS group. The enhanced bone mineralization and formation of bone trabeculae further supported these findings, indicating more favorable outcomes. Masson's staining revealed that the bone defect area of the TBS Group had significantly more mature bone tissue than the Control Group and BBS Group, with good cortical bone formation.

WB results of newly formed bone tissue (Fig. 5L–N) revealed notable enhancements in the levels of VEGF (0.32 ± 0.02 vs 0.13 ± 0.03, 0.40 ± 0.02 vs 0.13 ± 0.03) and BMP2 (0.51 ± 0.03 vs 0.08 ± 0.02, 0.86 ± 0.04 vs 0.08 ± 0.02) proteins in both the BBS Group and TBS Group, in comparison to the Control Group ($P < 0.05$). Additionally, the levels of VEGF and BMP2 in the TBS Group were higher than those in the BBS Group ($P < 0.05$).

The biomechanical testing results of the newly formed bone tissue (Fig. 5O) showed that compared to the Control group, the maximum failure force levels of BBS group and TBS group (70.10 ± 11.19 vs 25.37 ± 4.63, 168.47 ± 21.59 vs 25.37 ± 4.63) were significantly enhanced ($P < 0.05$). Furthermore, the maximum failure force in the TBS group was higher than that in the BBS group ($P < 0.01$).

Discussion

In this study, we developed a 3D-printed HA/CMCS/PDA/TFRD porous scaffold with the majority of pore sizes around 600–800 μm, exhibiting good degradation and drug release performance. The in vitro experiments demonstrated that the scaffold extracts facilitated the osteogenic differentiation of BMSCs, as evidenced by increased ALP activity, positive ARS staining, and the upregulation of osteogenic genes and proteins such as Runx2, OCN, and BMP2. The scaffold extracts also stimulated cell migration and vascular formation in HUVECs, accompanied by increased levels of PI3K, AKT, HIF-1a, VEGF mRNA, and proteins. In animal experiments, the scaffold demonstrated good biocompatibility, as evidenced by inhibition of infection and inflammation markers and nontoxic effects on liver and kidney function. Moreover, the scaffold exhibited favorable effects on promoting osteogenesis and angiogenesis in bone defects, as observed through X-ray, micro-CT analysis, and histological examination, indicating bone repair and vascular generation. Immunohistochemical analysis showed high expression of CD31 and BMP2, while WB analysis revealed elevated levels of BMP2 and VEGF protein expression. Mechanical testing showed that the scaffold significantly enhanced the maximum failure force of new bone tissue.

The design of a scaffold for bone regeneration requires meeting requirements such as degradation, porosity, and biocompatibility[33]. CMCS, PDA, and TFRD are easily decompose and disappear. HA, as the main inorganic component of human skeletal tissue, can be absorbed by the body, making it widely used in biomaterials[34]. Chen *et al*.[25] found that HA scaffold had a degradation rate of 17% at 10 weeks, with the pH decreasing from 7.4 to 7.0 in PBS simulated body fluid for 5 days and then slowly increasing. In our study, the HA/CMCS/PDA/TFRD scaffold had a degradation rate of 18.53% at 12 weeks, with a pH value of 7.00 ± 0.13, similar to the previous study. Furthermore, drug release reached its peak at 12 h and gradually decreased thereafter. Regarding porosity, it has been reported that an ideal scaffold should have a porosity range of 60–90% with pore sizes larger than 150 μm, providing a conducive environment for cell attachment and growth[33]. The porous scaffold we designed meets these requirements, with pore sizes around 600–800 μm, providing a growth channel for cells. Biocompatibility refers to the various reactions between materials and organisms due to their interactions, including biological, physical, and chemical aspects. It has been found that bFGF-modified HA scaffolds combined with BMP-2 exhibit good biocompatibility in vitro and in vivo, promoting healing of rabbit mandibular bone defects[35]. We found that the TBS Group and BBS Group showed similar trends in infection and inflammation markers (WBC, NEU%, PLT, IL-1, IL-6, TNF-α), liver function (AST, ALT, ALB), and kidney function (Cre, UREA, P) at 1, 3, 7, and 14 days postoperatively. Pathological examination also indicated no hepatorenal toxicity of the scaffold. Interestingly, the TBS Group may have certain anti-inflammatory effects, reflected in the reduction of postoperative WBC, IL-1, and IL-6. These findings establish a basis for the expanded utilization of the HA/CMCS/PDA/TFRD porous scaffold in various applications.

Previous studies have suggested that bone repair involves two simultaneous processes: vascular regeneration and bone formation. Vascular regeneration includes blood vessel migration and neovascularization, while bone formation involves the synthesis of bone matrix and mineralization[36]. Blood vessels were necessary for transporting nutrients, oxygen, minerals, and metabolic

waste required for osteoblast bone matrix synthesis and mineralization[37]. Therefore, the design of a scaffold for bone repair often considers inducing vascular generation and bone formation. In our study, due to the opaqueness of the scaffold, the microscope was unable to capture the cells within the scaffold pores clearly. Therefore, we prepared scaffold extracts based on previous studies to evaluate their angiogenic and osteogenic efficacy[38]. The results showed that the scaffold extract enhanced the ALP activity and positive ARS staining of BMSCs, promoting the expression of osteogenic genes and proteins (Runx2, OCN, and BMP2). It also stimulated cell migration and vascular formation in HUVECs, accompanied by increased levels of PI3K, AKT, HIF-1a, VEGF mRNA, and proteins. However, this effect was abolished by the phosphoinositide 3-kinase (PI3K) inhibitor LY294002. This is similar to our previous findings that TFRD can promote cell migration and vascular formation in HUVECs, possibly through PI3K/AKT signaling pathway[31,39]. Lv *et al.* loaded TFRD on a hydrogel scaffold and found that TFRD promoted ALP expression and matrix mineralization, enhancing osteogenic ability of the cells[40]. However, the use of HA to load TFRD has not been reported yet. Nevertheless, there are previous reports on the use of HA to load herbal ingredients and its application in cells and bone defects. For example, Li *et al.*[12] found that HA-loaded gastrodin, an active component of herbal medicine, upregulated the expression levels of osteogenic factors, specifically BMP-2 and ALP, in rat BMSCs, and angiogenic factors (VEGF and BFGF) in HUVECs, promoting vascular formation and bone formation in rat femoral condyle defects. Additionally, the PI3K/Akt signaling pathway has been shown to regulate vascular generation and bone formation in a mouse model of postmenopausal osteoporosis[41]. Lv *et al.*[42] found that TFRD activated the PI3K/AKT pathway in osteoblasts to promote proliferation, inhibit apoptosis, and reduce ROS levels. Huang *et al.*[43] also found that TFRD facilitated the osteogenic differentiation of rat dental pulp stem cells through the PI3K/Akt pathway in a concentration-dependent and time-dependent manner. Interestingly, our in vitro experiments also demonstrated that the scaffold extract of HA/CMCS/PDA/TFRD can promote vascular generation and bone formation, possibly through the regulation of the PI3K/AKT pathway.

Many previous studies have only evaluated the bone repair effects of various biomaterials on local bone defects, which has limited value for clinical reference. Segmental bone defects present a challenge for clinical doctors and patients because they involve long defect distances, slow bone formation, and lengthy repair periods, with few long-term observational studies available. In our study, we simulated the clinical scenario of segmental bone defects and constructed a 4 mm rat tibial bone defect model to observe the long-term effects of TFRD-loaded scaffolds in a preclinical setting. The 4 mm bone defect in rats is a simulated clinical segmental bone defect model, which has been proven to be difficult to heal through autogenous healing within a short period of time. It is currently commonly used as a model to evaluate the effectiveness of bone-inducing materials, distraction osteogenesis and induced membrane technique in promoting bone regeneration[44,45]. After 12 weeks of implantation, X-ray analysis revealed significant mineralization of rat tibial bones in the scaffold loaded with TFRD. Micro-CT analysis showed improved bone microstructure parameters (TMD, BV/TV), and histological staining (HE, Safranin O, Masson) demonstrated a significantly higher presence of mature bone tissue in the defect area compared to the scaffold without TFRD. The expression of BMP2 in the bone defect area also increased. Additionally, increased vascularization was observed through angiography, and the expression of CD31, as well as VEGF and BMP2 proteins, was significantly elevated, consistent with previous studies[39]. HA, as one of the components of the scaffold, has been proven to promote bone repair. For instance, Jiang *et al.*[46] found that HA scaffolds not only exhibited good biocompatibility but also enhanced the expression of BMP-2 and VEGF, demonstrating their potential for angiogenesis and osteogenesis. Feng *et al.*[47] discovered that HA not only possessed certain mechanical properties but also observed vascularized bone regeneration in critical bone defects in rats and rabbits. Similarly, TFRD has also been shown to promote bone repair. Shen *et al.*[48] found that TFRD showed a trend in repairing segmental tibial bone defects in rats through local administration and oral gavage in short-term observations. Jin *et al.*[49] discovered that injectable bone repair materials combined with TFRD could promote the repair of rat cranial bone defects. However, we found that vascular formation was significantly less than the results reported at 8 weeks post-surgery, which may be due to the early increase in blood vessels providing material transport for bone repair. As bone repair progresses, the local energy demand decreases, leading to the gradual disappearance of capillaries[50]. Furthermore, although TFRD could increase the maximum failure force of the newly formed bone tissue, it was still significantly lower than the level of normal bone tissue. This could be attributed to the short post-operative time, indicating that bone remodeling has not been fully completed, resulting in a lower axial load capacity of the bone. Therefore, the scaffold loaded with TFRD was confirmed to promote local vascular generation in bone defects, thereby facilitating the synthesis and mineralization of bone matrix and providing a possibility for localized drug delivery to address low patient compliance associated with long-term oral medications. Compared to distraction osteogenesis, our scaffold reduced the long-term slow distraction process and the risk of infection[44]. Additionally, it avoids the need for a secondary surgery associated with induced membrane technique and prevents the rejection reactions between different donors associated with collagen scaffold[44,51].

This study has some limitations. Firstly, when evaluating the degradation performance, we did not further analyze the changes within the first 2 weeks. Some studies have suggested that the pH value changes within 2 weeks initially decrease and then increase, but our study did not observe this phenomenon due to the lack of time segmentation. Secondly, direct cell culture on the porous scaffold was not performed. Preliminary experiments failed to observe cell growth on the scaffold under a microscope, and since our study mainly focused on the effect of drug loading on cells, we prepared scaffold extracts for in vitro experiments.

Conclusion

Inspired by the local application of TFRD to cure fracture, a 3D printed HA/CMCS/PDA/TFRD scaffold with anti-infection, biodegradability, angiogenesis, and osteogenesis was designed, and preclinical evaluation was made in segmental bone defect. This scaffold provided a conducive microenvironment for cell proliferation and migration, significantly promoting bone and vascular formation, as confirmed by in vitro cell experiments.

Furthermore, in vivo experiments demonstrated that the microchannel-rich scaffold exhibited excellent vascularization capacity and osteogenic performance at the site of rat segmental tibial bone defects, resulting in effective bone regeneration. This study provides a prospective strategy for bone regeneration by combining biomimetic microstructures and drug delivery.

Ethical approval

Ethical approval for this study (Ethical Committee GZTCMF1-2021020) was provided by the Ethical Committee of the First Affiliated Hospital of Guangzhou University of Chinese Medicine, Guangzhou, China on 10 April 2021.

Consent

N/A.

Sources of funding

This work was supported, in part, by National Natural Science Foundation of China (No. 81974575), Special Funds for the Discipline Reserve Talent Cultivation Project of Guangzhou University of Chinese Medicine 'Double First-Class' and High-level University Construction, and Cultivation of Young and Middle-aged Talents in the First Affiliated Hospital of Guangzhou University of Chinese medicine (2023), Huang Feng National Famous Traditional Chinese Medicine Expert Inheritance Studio. The study sponsor had no involvement in this study, such as the collection, analysis and interpretation of data; the writing of the manuscript; and the decision to submit the manuscript for publication.

Author contribution

H.X.L.: conceptualization; H.X.L. and Z.G.L.: data analysis; H.X.L., Z.G.L., Z.Z.X., S.Y.T., M.L.H., Y.H.W., Z.S., R.Y.Z., J. J.F., Y.L.F., H.M.C., and Y.Y.R.: methodology; X.T.W.: project administration; F.H., Z.W.J.: supervision; H.X.L., X.T.W., and Z.W.J.: writing, review and editing. All authors contributed constructive comments on the paper.

Conflicts of interest disclosure

N/A.

Research registration unique identifying number (UIN)

This study does not involve humans and does not require clinical ethics approval or clinical trial registration.

Guarantor

ZW Jiang.

Data availability statement

Data will be provided upon reasonable request.

Provenance and peer review

Not commissioned, externally peer-reviewed.

References

[1] Wei H, Cui J, Lin K, *et al*. Recent advances in smart stimuli-responsive biomaterials for bone therapeutics and regeneration. Bone Res 2022;10:17.
[2] Gubin A, Borzunov D, Malkova T. Ilizarov method for bone lengthening and defect management review of contemporary literature. Bull Hosp Jt Dis 2013;2016:145–54.
[3] Pereira R, Perry WC, Crisologo PA, *et al*. Membrane-induced technique for the management of combined soft tissue and osseous defects. Clin Podiatr Med Surg 2021;38:99–110.
[4] Chappell AG, Ramsey MD, Dabestani PJ, *et al*. Vascularized bone graft reconstruction for upper extremity defects: a review. Arch Plast Surg 2023;50:82–95.
[5] Kawecki F, L'Heureux N. Current biofabrication methods for vascular tissue engineering and an introduction to biological textiles. Biofabrication 2023;15:22004.
[6] Zhang T, Wei Q, Zhou H, *et al*. Three-dimensional-printed individualized porous implants: a new "implant-bone" interface fusion concept for large bone defect treatment. Bioact Mater 2021;6:3659–70.
[7] Zhang T, Wei Q, Zhou H, *et al*. Sustainable release of vancomycin from micro-arc oxidised 3D-printed porous Ti6Al4V for treating methicillin-resistant Staphylococcus aureus bone infection and enhancing osteogenesis in a rabbit tibia osteomyelitis model. Biomater Sci 2020;8:3106–15.
[8] Zhang M, Matinlinna JP, Tsoi J, *et al*. Recent developments in biomaterials for long-bone segmental defect reconstruction: a narrative overview. J Orthop Translat 2020;22:26–33.
[9] Horstmann PF, Raina DB, Isaksson H, *et al*. Composite biomaterial as a carrier for bone-active substances for metaphyseal tibial bone defect reconstruction in rats. Tissue Eng Part A 2017;23:1403–12.
[10] Guo T, Yuan X, Li X, *et al*. Bone regeneration of mouse critical-sized calvarial defects with human mesenchymal stem cell sheets co-expressing BMP2 and VEGF. J Dent Sci 2023;18:135–44.
[11] Lin H, Wang X, Huang M, *et al*. Research hotspots and trends of bone defects based on Web of Science: a bibliometric analysis. J Orthop Surg Res 2020;15:463.
[12] Li L, Li Q, Gui L, *et al*. Sequential gastrodin release PU/n-HA composite scaffolds reprogram macrophages for improved osteogenesis and angiogenesis. Bioact Mater 2023;19:24–37.
[13] Zeng Z, Huang F, Li Y, *et al*. Effect of total flavonoids of rhizoma drynariae on masquelet-induced membrane angiogenesis factor expression in rats. Chinese Arch Traditional Chinese Med 2019;37:2345–8.
[14] Li S, Zhou Q, Zhou H, *et al*. Clinical observation on treatment of infectious osteomyelitis with bone defect by Qianggu capsule and induction membrane technique. Shandong Medical Journal 2019;59:73–6.
[15] Oryan A, Alidadi S, Bigham-Sadegh A, *et al*. Effectiveness of tissue engineered chitosan-gelatin composite scaffold loaded with human platelet gel in regeneration of critical sized radial bone defect in rat. J Control Release 2017;254:65–74.
[16] Maji S, Agarwal T, Das J, *et al*. Development of gelatin/carboxymethyl chitosan/nano-hydroxyapatite composite 3D macroporous scaffold for bone tissue engineering applications. Carbohydr Polym 2018;189:115–25.
[17] Shi X, Wu Y, Xu Y. Research progress of biomaterial scaffolds in repairing infectious bone defects. Orthop Biomechanics Materials Clin Study 2022;19:80–4.
[18] Fan Y, Zhang Y, Zhao Q, *et al*. Immobilization of nano Cu-MOFs with polydopamine coating for adaptable gasotransmitter generation and copper ion delivery on cardiovascular stents. Biomaterials 2019;204:36–45.
[19] Cui T, Yu J, Wang CF, *et al*. Micro-gel ensembles for accelerated healing of chronic wound via pH regulation. Adv Sci (Weinh) 2022;9:e2201254.
[20] Zhang H, Cui Y, Zhuo X, *et al*. Biological fixation of bioactive bone cement in vertebroplasty: the first clinical investigation of borosilicate glass (BSG) reinforced PMMA bone cement. ACS Appl Mater Interfaces 2022;14:51711–27.
[21] Kilkenny C, Browne WJ, Cuthill IC, *et al*. Improving bioscience research reporting: the ARRIVE guidelines for reporting animal research. PLoS Biol 2010;8:e1000412.

[22] Wang X, Wang C, Wang X, *et al*. A polydopamine nanoparticle-knotted poly(ethylene glycol) hydrogel for on-demand drug delivery and chemo-photothermal therapy. Chemistry Materials 2017;29:1370–6.
[23] Su Y, Pan H, Liu D, *et al*. Advances in polydopamine-based drug delivery systems for tumor targeting. Acta Pharmaceutica Sinica 2022;57:25–35.
[24] Yang H, Hao L, Du C, *et al*. A systematic examination of the morphology of hydroxyapatite in the presence of citrate. RAC Advances 2013;45: 23184–9.
[25] Chen T, Zou Q, Du C, *et al*. Biodegradable 3D printed HA/CMCS/PDA scaffold for repairing lacunar bone defect. Mater Sci Eng C Mater Biol Appl 2020;116:111148.
[26] Xie J, Li C, Hong S, *et al*. In vitro drug release test of electrospun drug-loaded nanofibrous membrane by using ultraviolet-visible spectrophotometer method. China Fiber Inspection 2013;9:82–5.
[27] Wang C, Lin K, Chang J, *et al*. Osteogenesis and angiogenesis induced by porous beta-CaSiO(3)/PDLGA composite scaffold via activation of AMPK/ERK1/2 and PI3K/Akt pathways. Biomaterials 2013;34:64–77.
[28] Chen J, Zhou X, Sun W, *et al*. Vascular derived ECM improves therapeutic index of BMP-2 and drives vascularized bone regeneration. Small 2022;18:e2107991.
[29] He Y, Li F, Jiang P, *et al*. Remote control of the recruitment and capture of endogenous stem cells by ultrasound for in situ repair of bone defects. Bioact Mater 2023;21:223–38.
[30] Wu Q, Xu S, Wang X, *et al*. Complementary and synergistic effects on osteogenic and angiogenic properties of copper-incorporated silicocarnotite bioceramic: in vitro and in vivo studies. Biomaterials 2021;268:120553.
[31] Lin H, Wang X, Li Z, *et al*. Total flavonoids of Rhizoma drynariae promote angiogenesis and osteogenesis in bone defects. Phytother Res 2022;36:3584–600.
[32] Lane JM, Sandhu HS. Current approaches to experimental bone grafting. Orthop Clin North Am 1987;18:213–25.
[33] Ravoor J, Thangavel M, Elsen S R. Comprehensive review on design and manufacturing of bio-scaffolds for bone reconstruction. ACS Appl Bio Mater 2021;4:8129–58.
[34] Kavitha SA, Arthi C, Neya NR, *et al*. Nano-hydroxyapatite/collagen composite as scaffold material for bone regeneration. Biomed Mater 2023;18:32002.
[35] Cai Y. Study on biocompatibility of two-factor bFGF/BMP-2/nHAP/COL scaffold in vivo and in vitro. China Medical University; 2018. PhD's Thesis, 95.
[36] Xie H, Cui Z, Wang L, *et al*. PDGF-BB secreted by preosteoclasts induces angiogenesis during coupling with osteogenesis. Nat Med 2014;20: 1270–8.
[37] Carmeliet P, Jain RK. Molecular mechanisms and clinical applications of angiogenesis. Nature 2011;473:298–307.
[38] Gu Y, Zhang J, Zhang X, *et al*. Three-dimensional Printed Mg-Doped beta-TCP bone tissue engineering scaffolds: effects of magnesium ion concentration on osteogenesis and angiogenesis in vitro. Tissue Eng Regen Med 2019;16:415–29.
[39] Shen Z, Dong W, Chen Z, *et al*. Total flavonoids of Rhizoma Drynariae enhances $CD31^{(hi)}Emcn^{(hi)}$ vessel formation and subsequent bone regeneration in rat models of distraction osteogenesis by activating PDGF-BB/VEGF/RUNX2/OSX signaling axis. Int J Mol Med 2022;50: 112.
[40] Lv L, Cheng W, Wang S, *et al*. Poly(beta-amino ester) dual-drug-loaded hydrogels with antibacterial and osteogenic properties for bone repair. ACS Biomater Sci Eng 2023;9:1976–90.
[41] Abdurahman A, Li X, Li J, *et al*. Loading-driven PI3K/Akt signaling and erythropoiesis enhanced angiogenesis and osteogenesis in a post-menopausal osteoporosis mouse model. Bone 2022;157:116346.
[42] Lv W, Yu M, Yang Q, *et al*. Total flavonoids of Rhizoma drynariae ameliorate steroid-induced avascular necrosis of the femoral head via the PI3K/AKT pathway. Mol Med Rep 2021;23:345.
[43] Huang X, Yuan S, Yang C. Effects of drynaria total flavonoid on osteogenic differentiation of rat dental pulp stem cells via PI3K/Akt pathway. Chin J Tissue Engineering Res 2013;17:92–7.
[44] Shen Z, Lin H, Chen G, *et al*. Comparison between the induced membrane technique and distraction osteogenesis in treating segmental bone defects: an experimental study in a rat model. PLoS One 2019;14: e226839.
[45] Lin S, Maekawa H, Moeinzadeh S, *et al*. An osteoinductive and biodegradable intramedullary implant accelerates bone healing and mitigates complications of bone transport in male rats. Nat Commun 2023;14: 4455.
[46] Jiang J, Liu W, Xiong Z, *et al*. Effects of biomimetic hydroxyapatite coatings on osteoimmunomodulation. Biomater Adv 2022;134:112640.
[47] Feng C, Xue J, Yu X, *et al*. Co-inspired hydroxyapatite-based scaffolds for vascularized bone regeneration. Acta Biomater 2021;119:419–31.
[48] Shen Z, Guo Y, Jiang Z, *et al*. Comparison of the effects between two routes of total flavones of Rhizoma Drynariae administration on large segmental bone defects in rats based on bone tissue engineering technique. Chin J Tissue Engineer Res 2022;26:4346–52.
[49] Jin H, Li J, Yu X, *et al*. Analysis on the effect of the application of IBRC in combination with AFDR in the rapair of Maximal rat skull defect. Orthop Biomechan Materials Clin Study 2012;9:26–9.
[50] Huang C. A study on the role and mechanism of H-type blood vessels in the repair of segmental bone defect of femur in rat. Guangzhou Medical University; 2020. Master's Thesis, 64.
[51] Dec P, Modrzejewski A, Pawlik A. Existing and novel biomaterials for bone tissue engineering. Int J Mol Sci 2022;24:529.